International Journal of Heat and Mass Transfer 180 (2021) 121760

Contents lists available at ScienceDirect

International Journal of Heat and Mass Transfer

journal homepage: www.elsevier.com/locate/hmt

Spatially periodic vapor bubble activity during subcooled pool boiling on 1D aluminum alloy micro-fin arrays

Brendon Doran[a,b], Bin Zhang[c], Shayan Davani[a], Kojo Asiamah Osafo[d], Owen Sutka[a,e], Abigail Walker[a,b], Nicholas Mueller[a,b], Stephen Akwaboa[d], Patrick Mensah[d], W.J. Meng[c], Arden L. Moore[a,b,*]

[a] *Institute for Micromanufacturing, Louisiana Tech University, Ruston, LA 71272, USA*
[b] *Mechanical Engineering Dept., Louisiana Tech University, Ruston, LA 71272, USA*
[c] *Mechanical & Industrial Engineering Dept., Louisiana State University, Baton Rouge, LA 70803, USA*
[d] *Mechanical Engineering Dept., Southern University, Baton Rouge, LA 70813, USA*
[e] *Electrical Engineering Dept., Louisiana Tech University, Ruston, LA 71272, USA*

ARTICLE INFO

Article history:
Received 30 March 2021
Revised 7 July 2021
Accepted 19 July 2021

Keywords:
Pool boiling
Microstructures
Phase change
Microfins

ABSTRACT

Within the broad field of micro- and nano- scale surface modification to improve pool boiling performance, micro-fin arrays are especially attractive due to their ability to significantly increase wetted surface area with minimal increase in size or weight compared to macroscopic fins. In addition, their regular and repeating geometry enables greater potential for parametric optimization, uniformity, and repeatability as compared to more randomized alternatives. However, the presence of a regular, repeating microscale pattern on a heated surface has previously been shown to create alternating regions of liquid and vapor flow at small length scales which can strongly affect the macroscopic heat transfer performance of the surface. In this work, a combination of pool boiling experiments, high-speed imaging, and numerical modeling were used to investigate vapor bubble behavior and pool boiling heat transfer characteristics from one-dimensional (1D) aluminum alloy micro-fin arrays in the dielectric coolant HFE-7100. Results showed that the presence of 1D micro-fin arrays can significantly enhance pool boiling performance above that of a planar, unpatterned baseline surface but with important and sometimes nonintuitive dependence on micro-fin height. Experimental data indicated that a simple increase in surface area does not necessarily correlate to improved heat transfer performance, while high-speed imaging revealed that the presence of the micro-fins induces a periodic series of upward and downward flow patterns, in addition to distinct vapor bubble migration behavior. These results expand the range of surface types and working fluids for which spatially periodic and distinct liquid/vapor transport pathways created via microscale surface modification have been reported.

1. Introduction

Pool boiling plays a vital role in many activities with wide societal impact including food processing, power generation, chemical production, and manufacturing. In these areas, it is often desirable to maximize the heat transfer performance of the working surface in order to optimize efficiency, reduce size/weight/cost, and improve long-term reliability of both the process and its associated hardware. Artificial surface roughening to promote nucleation and the addition of macroscopic fin structures to increase surface area have historically been the most utilized methods for achieving such enhancements and continue to be relied upon today. More recently, the development of advanced surface modification capabilities via micro-fabrication, nanomaterials coatings, and controllable superhydrophobicity/philicity has inspired phase change heat transfer researchers to leverage these scientific advancements to push the bounds of pool boiling process performance beyond the limits of traditional surface enhancements techniques [1–4].

Within the broad field of micro- and nanoscale surface modification, micro-fin arrays (MFAs) are an especially attractive means of enhancing pool boiling for several reasons. First, their microscale features facilitate significant increases of wetted surface area with minimal increase in size or weight compared to macroscopic fins. Second, modern manufacturing techniques can provide a high

* Corresponding author: Institute for Micromanufacturing, Louisiana Tech University, Ruston, LA 71272, USA.
E-mail address: amoore@latech.edu (A.L. Moore).

https://doi.org/10.1016/j.ijheatmasstransfer.2021.121760
0017-9310/

degree of control over micro-fin shape, size, and spacing. This, in turn, enables greater potential for parametric optimization, uniformity, and repeatability compared to more randomized alternatives to surface modification such as abrasion, open cell foams, or particulate coatings. In addition, MFAs may be able to provide better long-term performance stability than coatings or chemical modifications alone, where the potential for detachment, denaturing, or fouling over time is a major concern [5,6]. These advantages have motivated a significant number of studies on pool boiling phenomena from MFAs of varying materials and geometries across a spectrum of working fluids, the major results of which have been excellently reviewed previously [7,8] and have consistently shown enhancements in nucleate pool boiling performance and critical heat flux (CHF) compared to unpatterned surfaces.

However, there are still several pressing scientific and technological issues which limit the widespread adoption of MFAs outside of a laboratory environment. Despite their obvious ability to enhance wetted surface area, the actual physics behind pool boiling from surfaces with microstructuring can be quite complex. When micro-fin features become comparable to the sub-millimeter sizes relevant to individual bubble ebullition cycles, multifaceted flow behaviors can result that make *a priori* optimization of an MFA design for a given operating environment much more complicated than simply maximizing surface area. For example, a series of works from the Kandlikar group [9–15] have shown that open micro-channels can result in distinctly different liquid and vapor transport pathways along the surface. In the absence of nucleation-promoting coatings, the micro-channels themselves were reported to act primarily as liquid resupply pathways while bubble growth and departure occurred preferentially from the tops of the micro-channels [9,10,12,14]. The overall effect is alternating regions of downward liquid flow and upward vapor flow, the specific behaviors of which are dictated by the micro-channel geometry. Rahman et al. [16] achieved similar spatially alternating liquid and vapor transport regions by manipulating instead the thermal conductivity variation of the heated surface, and in doing so achieved 5x enhancement in heat transfer rate.

These works have demonstrated the intriguing possibility of manipulating liquid and vapor dynamics at their natural sub-millimeter dimensional scales such as capillary length and bubble diameter, and by doing so enhancing the heat transfer performance far beyond what simple surface area increases could offer. However, this complex phenomenon of spatially periodic liquid and vapor transport pathways induced by microscale surface engineering is in need of much more detailed study if the scientific and engineering communities are to be able to leverage it fully and achieve surface optimization by *a priori* design rather than by systematic trial-and-error. In particular, the previous works in this area [9,10,12,14,16] have focused almost exclusively on water. Thermophysical properties such as surface tension and density are particularly important in influencing bubble size and capillary action, as well as nucleation behavior. Thus, there is a strong need to determine how this spatially periodic multiphase transport behavior translates to other working fluids such as the low surface tension dielectric coolants utilized in immersion cooling [4,17–20]. Further, these existing studies have utilized relatively simple microscale geometries such as vertical sidewall micro-channels [9,10,12,14] or rectangular strips of low thermal conductivity material [16]. In both cases, the boundaries between the alternating rectangular geometric regions were clearly defined. It is thus unclear whether other microscale surface geometries might produce similar multiphase behavior.

In this work, a combination of high-speed imaging, pool boiling experiments, and numerical modeling is used to investigate vapor bubble behavior and pool boiling heat transfer characteristics from 1D aluminum (Al) alloy MFAs in a non-aqueous working fluid. The obtained results expand the range of surface types and working fluids for which spatially periodic and distinct liquid/vapor transport pathways created via microscale surface modification have been reported. Additional analysis of observed vapor bubble behavior and preferential nucleation site activity is utilized to refine hypotheses about the underlying physical mechanisms which drive the formation of such multiphase behavior. Importantly, the 1D Al alloy MFAs in this work are created via a high-throughput roll molding technique and possess superior scalability compared to other MFA fabrication methods. With data supporting their ability to effectively enhance heat transfer, MFAs created through this approach address a key issue often cited as limiting the industrial adoption of micro/nanoscale surface modifiers [5].

2. Material and methods

2.1. Fabrication and characterization of 1D MFAs fabricated by high throughput roll molding

Rolling molding of Al strips was conducted using a custom-designed and built machine, analogous to those used for sheet metal rolling [21]. In the present work, the roller sleeves, made of hardened 52,100 steel, have a total width of 25.4 mm and contain an array of circumferential micro-protrusions. The protrusion sidewalls possess a slight taper of approximately 7°. More details of the rolling machine and roller sleeves have been published elsewhere [22]. Commercial Al 1100 (99% + Al) sheet metal strips were used as substrates. The Al strips had an initial thickness of ~6.35 mm and an initial width of ~31.8 mm. Prior to rolling, Al strips were annealed at 300 °C for 12 h. After rolling, the inverse of the protrusion patterns was imprinted onto the Al strips surfaces, forming an array of micro-fin structures. Our previous experiments showed that the height of the formed micro-fins scaled almost linearly with the normal load applied onto the Al strip [23]. In the present experiment, micro-fins with three different heights were achieved by varying this normal load. Following roll-molding, each patterned strip was cut at lengths of 25.4 mm and widths of 25.4 mm to create multiple square samples of each type. The total thickness of the samples was thinned to be ~1 mm via removal of excess base material from the backside.

Micro-fin height measurement and morphological examinations of roll molded Al specimens were conducted through scanning electron microscopy (SEM) on an FEI Quanta3D FEG DaulBeam focused ion beam (FIB) instrument, with representative results shown in **Fig. 1**. It is important to note that the pattern pitch, micro-fin width at the base, and channel width at the base are all dictated by the dimensions of the master roller sleeve. Since the same master roller sleeve was used for all samples, these parameters are nearly identical amongst the three sample types as shown in **Fig. 1**. However, the micro-fin height and micro-fin width at the top are dependent on the applied normal load force, with a greater force resulting in a taller micro-fin with reduced topmost width. Important MFA dimensional values for the three levels of applied force are summarized in **Table 1** below, which also includes the increase in wetted surface area achieved relative to a planar baseline sample of identical 25.4 x 25.4 mm footprint. The trapezoidal cross-sectional geometry and curved micro-fin top are important to note, as they represent deviations in microscale surface modification from those that have previously been reported [9,10,12,14,16] to induce distinct liquid and vapor transport pathways. For the MFAs in this work, the boundaries between the alternating rectangular geometric regions are less clearly defined by comparison. It was thus unclear prior to testing whether they might produce similar multiphase behavior.

One of the challenges associated with MFA pool boiling studies is the relatively large number of geometric attributes which may

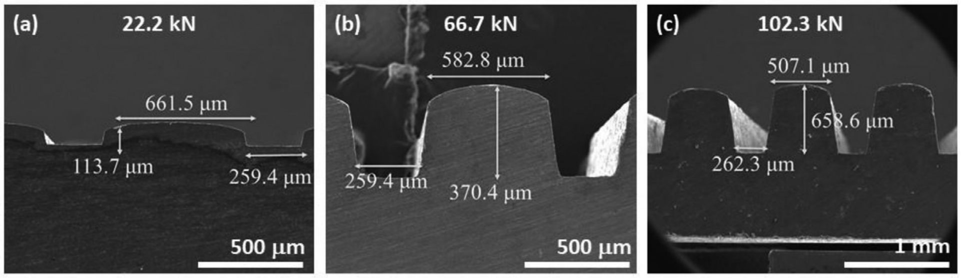

Fig. 1. SEM cross-sectional images of the micro-fin geometries obtained by roll molding at (a) 22.2 kN, (b) 66.7 kN, and (c) 102.3 kN applied force.

Table 1
Summary of MFA geometries as observed via SEM imaging. This table also includes the increase in wetted surface area relative to a planar baseline sample of identical 25.4 x 25.4 mm footprint.

Sample Type	**Applied Force (kN)**	**Micro-Fin Height (μm)**	**Micro-Fin Width at Top (μm)**	**Pitch (μm)**	**Total Number of Fins**	**Surface Area Increase**
Planar	–	–	–	–	0	1x (baseline)
MFA1	22.2	113.7	661.5	953.9	26	1.25x
MFA2	66.7	370.4	582.8	959.8	26	1.88x
MFA3	102.3	658.6	507.1	955.4	26	2.71x

be varied, such as micro-fin height, width, spacing/pitch, configuration, and shape. Here, we wish to focus on those geometric variables that have been shown in literature to most strongly influence pool boiling or which are most likely to lead to spatially periodic and distinct liquid/vapor transport pathways. Previous studies have highlighted the micro-fin height (or, similarly, micro-channel depth) as having one of the strongest influences on the overall surface performance of MFAs in pool boiling [15,24–27]. As shown in **Table 1** the range of micro-fin heights was much greater than the variation in micro-fin width with applied force, which makes micro-fin height the primary variable related to pool boiling performance of these MFAs. The limited previous works on spatially periodic and distinct liquid/vapor transport pathways created via microscale surface modification have highlighted pitch as another important variable. Specifically, Rahman et al. [16] showed that the greatest heat transfer coefficient enhancement for their low thermal conductivity-patterned surfaces occurred when the square root of the Bond number (Bo_P) as defined in **Eq. (1)** was near unity, that is

$$Bo_P^{1/2} = \frac{P}{\lambda_C} \sim 1, \tag{1}$$

where P is the pitch of the pattern (corresponding to superheat variation wavelength along the surface) and λ_C is the capillary length of the working fluid as given by

$$\lambda_C = \sqrt{\frac{\sigma}{g(\rho_l - \rho_v)}}. \tag{2}$$

In **Eq. (2)**, g is the gravitational constant, σ is surface tension, and ρ_l and ρ_v are the densities of the liquid and vapor phases, respectively. Thus, the pattern pitch P which is expected to give the greatest heat transfer coefficient enhancement is dependent on the thermophysical properties of the working fluid. For water, the dominant working fluid within the literature, λ_C has a value of approximately 2.7 mm. In comparison, for low surface-tension dielectric coolants such as the Novec^{TM} HFE-7100 used in this work, λ_C is approximately 1.0 mm. Thus, the ~0.95 mm MFA pitch created by the master roller in this work is comparable to our working fluid's capillary length and, by virtue of **Eq. (1)**, the Bo_P value of greatest interest.

Surface roughness is known to play a significant role in nucleation activity, with nucleation site density being a strong influence on the pool boiling heat transfer performance of a given surface. Thus, it is important to quantify the surface roughness of the Al material pre- and post-rolling in order to determine if a significant change in surface roughness occurs as a result of the processing. The surface topology of planar non-rolled Al 1100 stock as well each of the MFA samples was collected using 3D laser scanning confocal microscopy (Keyence VK-X150). From area scan data shown in **Fig. 2**, the average roughness of the non-rolled stock was 3.2 μm. For the rolled MFA samples, the average roughness was 11.8 μm on micro-fin tops and 9.5 μm for the bottoms of channels, with no statistically significant difference in roughness based on applied rolling force. Thus, the roll molding process does create a greater surface roughness, although this increase is very small compared to the micro-fin features themselves and is consistent across MFA sample types.

2.2. Pool boiling performance testing

Pool boiling performance testing and data processing were performed as outlined in our previous publication [28] and the associated supplementary information, where full details of the experimental method and uncertainty analysis can be found. Briefly, the pool boiling setup shown schematically in **Fig. 3(a)** was utilized which allows for environmental control of the pool boiling environment as well as associated high-speed imaging. Immersed within the working fluid was a PTFE-based sample stage as shown in **Fig. 3(b)**. The interior copper block had two channels machined into its upper surface to accommodate a pair of K-type thermocouples (Omega) that were used to monitor temperature T_{base} on the backside of the sample during testing. During thermocouple installation, the thermocouple junctions were put in direct contact with the backside of the aluminum sample and held in place with OMEGABOND^{TM} 200 thermally conductive epoxy such that the epoxy's thermal resistance would not lie in series in between the junction and the aluminum. This was done to ensure that no subsequently large temperature difference would occur between the thermocouple junction and the backside of the aluminum sample. The desired condition was confirmed experimentally by touching a third thermocouple to the top of the sample and applying a heat flux of 5–10 W cm^{-2} via the stage prior to immersion in the tank. The temperature difference between the backside thermocouples and the temporary topside thermocouple was always found to be less than 0.5 °C, which was comparable to that expected for the aluminum alone via simple 1D thermal conduction

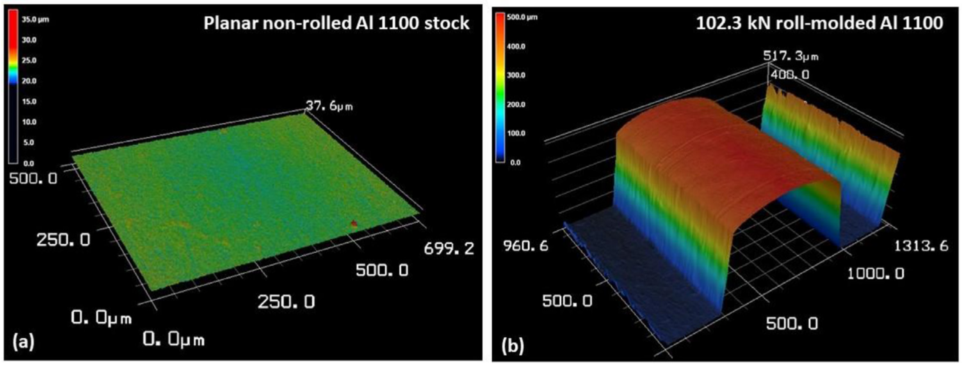

Fig. 2. Representative 3D laser scanning confocal topology mapping of (a) un-rolled Al 1100 stock and (b) the same material after roll-molding at 102.3 kN of applied force.

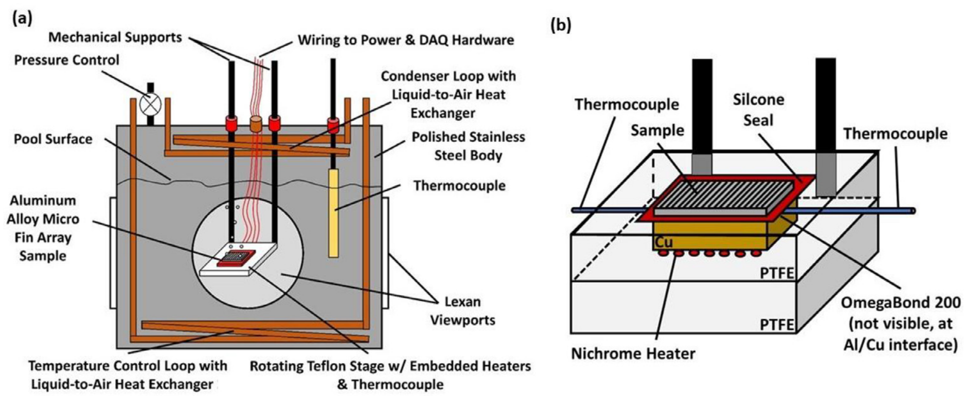

Fig. 3. Annotated illustrations of the experimental pool boiling setup, including (a) tank and (b) stage construction detail, with the topmost PTFE layer made semi-transparent to show the inner components. Not to scale.

analysis and indicated that there was not a significant additional thermal resistance present from epoxy or contact resistances.

A nichrome wire heater was adhered to the back of the copper heat spreader with OMEGABOND^{TM} 200 thermally conductive epoxy. The sample was surrounded by a second piece of PTFE with square cutout of the same dimensions as the sample base. All seams on the stage were sealed with thermally insulating PERMATEX^{TM} 81,160 high temperature RTV silicone. All thermocouples used in this work possessed an accuracy of +/- 2.1 °C per vendor specifications, and the worst-case parasitic heat loss from the sample stage through insulation, thermocouple wires, and power leads was estimated to be 2.5% of total power supplied via standard Kline-McClintock experimental uncertainty analysis [28,29].

The full computer-controlled testing procedure is described in detail in Ref. [28]. In terms of the pool boiling environment, an external liquid-to-air heat exchanger with closed-loop temperature control maintained a programmed setpoint for the pool while also serving the condensing coils, whose function was to maintain a constant liquid level throughout the experiment. Pool temperature was recorded at multiple locations via Type K thermocouples. The pressure within the tank was maintained at 1 atm throughout the experiment by an automated pressure control valve. Testing was conducted by increasing the applied heat flux until one of three events occurred: a) sample reached CHF, b) sample reached an average temperature of 100 °C, or c) the stage heater burned out.

The working fluid used in this work was the commercial dielectric coolant Novec^{TM} HFE-7100, which is one of several low surface tension dielectric fluids commonly utilized in immersion cooling of electronics. The Novec^{TM} HFE-7100 was degassed via repeated heating cycles prior to usage in final experiments. Despite the majority of pool boiling academic literature focusing on saturated boiling conditions, in this work we instead utilize a pool temperature that is essentially that of the ambient, specifically 21 °C. Because the saturation temperature for Novec^{TM} HFE-7100 is 61 °C at atmospheric pressure, this represents a significantly subcooled (ΔT_{sub} = 40 K) pool boiling environment. This was done to mimic industrial usage of the working fluid in which relatively large immersion containers also have access to external heat rejection infrastructure. In addition, it has been shown that subcooling can be highly effective in enhancing pool boiling performance and increasing the CHF [30–34], which further aids in ascertaining the upper limits of performance for the MFAs studied here. Further, the combined use of extended surfaces and subcooling has been explicitly cited as a viable means for cooling very high-power electronics [30].

During each pool boiling experiment, a high-speed camera (Phantom VEO 410, Vison Research) was used to capture images of bubble nucleation, coalescence, and movement over the MFA surface. A manual zoom lens (Resolv4K, Navitar) was mounted to the camera to assist the camera's digital zoom in order to maintain high resolution. The high-speed videos were recorded at frame rates ranging between 1000 and 4000 fps depending on the stage orientation and frame size (full frame or zoom). Besides flooding the tank with external illumination, the maximum available exposure time at each frame rate was used to obtain bright images. Image processing techniques were used to obtain bubble departure diameter statistics from the captured high-speed videos. These techniques, which were implemented via writing an automated algorithm in MATLAB, first separated the in-focus bubbles from unfocused ones in the background for a given image frame. The spherical nature of the departing bubbles facilitated the usage of a circu-

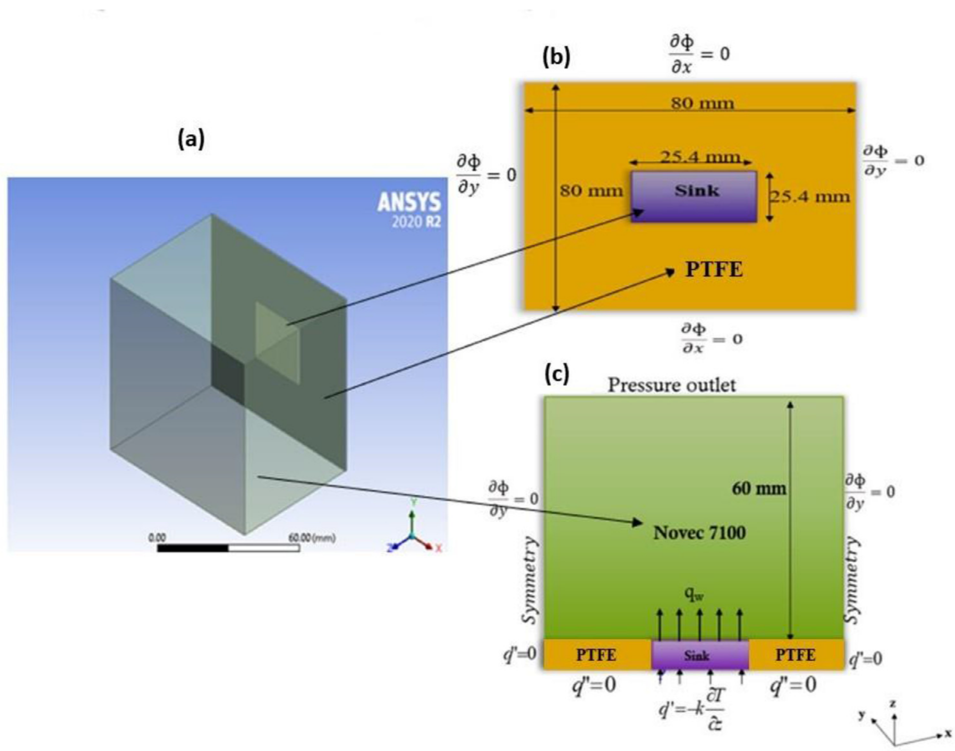

Fig. 4. Schematic of numerical modeling computational zones based on the experimental setup. (a) Close-up of the simulated stage area. (b) Top-down view annotated illustration of the stage area and its boundary conditions. (c) Side view annotated illustration of the computational domain and its boundary conditions.

lar Hough transform [35] for measuring bubble diameter. Approximately 30,000 individual frames from the high-speed videos were used for the analysis.

2.3. Numerical modeling

To help explain some of the flow characteristics observed during experiment, a numerical model was constructed which replicated the sample region shown in **Fig. 3** using ANSYS Design Modeler. This model is shown in **Fig. 4** below.

Fig. 4 shows the boundary conditions and physical inputs in the computational domain of the numerical model. The boundary conditions applied are mainly pressure outlet, wall and symmetry to mimic the experimental setup. It is assumed that the computational domain extents chosen for the simulation were far removed from the heat sink (which refers to the MFA under study) and PTFE insulation and hence symmetric boundary conditions can be enforced on the surroundings surfaces of Novec^{TM} HFE-7100 in the x-z and y-z planes. In **Fig. 4**, the symbol ϕ represents flow primitive variables including temperature and density. Pressure outlet boundary condition was applied to the top surface. The gauge pressure was set to 0, having a backflow turbulent intensity of 1% and backflow hydraulic diameter of 15.4 mm with a backflow total temperature of 334 K for both phases of Novec^{TM} HFE-7100. Heat fluxes were supplied to the sink wall boundary between q'' = 2.3 to 21.6 W cm^{-2}. All faces of PTFE are insulated (q''= 0) and so no heat flux is supplied at the PTFE wall boundary. All interphases were automatically generated as coupled interfacial walls with perfect thermal contact conditions (Novec^{TM}-sink, sink-PTFE and Novec^{TM} -PTFE interfaces.)

In order to solve the continuity, momentum, and energy equations in the quiescent natural convection environment, the numerical modeling approach adopted for this study was to use a built-in Eulerian multiphase boiling model (Rensselaer Polytechnic Institute model, RPI) available in ANSYS Fluent [37]. The RPI model is dependent on the boiling parameters which are bubble departure diameter, nucleation site density, frequency of bubble departure and area of influence coefficient. Through literature review [38,39,40] and our initial use of default ANSYS boiling parameters, it has been shown that boiling model parameters play a major role in heat dissipation in boiling systems. Hence, the built-in boiling parameters in ANSYS Fluent were augmented with a user-defined function developed in this study which replaced the nucleation site density model of Fincher [38] with the K-I model [39]. Results were validated against the planar Al experimental data from this work with good agreement within experimental uncertainty.

3. Results

Pool boiling performance data for the MFAs as well as for a baseline planar (i.e., unpatterned) sample of the same material are shown in **Fig. 5** for both horizontal and vertical stage orientations, with heat flux defined based on the projected base area of 25.4 x 25.4 mm. At least two separate samples of each MFA fin height were evaluated, and results were repeatable within experimental uncertainty over multiple runs on the same sample.

As shown in **Fig. 5**, for both orientations within the natural convection regime at low superheat ($\Delta T = T_{base} - T_{sat}$) values of ΔT less than −10 K, the heat transfer performance of all samples was comparable. For the horizontal stage orientation, differentiation between MFA sample types does not become strongly apparent until ΔT greater than 10 K at which point nucleate boiling was observed to have been well established via simultaneous imaging. Interestingly, for both orientations the MFAs with smallest fin height of 114 μm actually showed worse performance than the planar baseline samples despite their 1.25x greater surface area. In fact, two of the three 114 mm MFA samples were observed to be nearing CHF even at these relatively low superheat values as evidenced by their large temperature rise between data points. This is important as it illustrates that simply increasing surface area via microscale

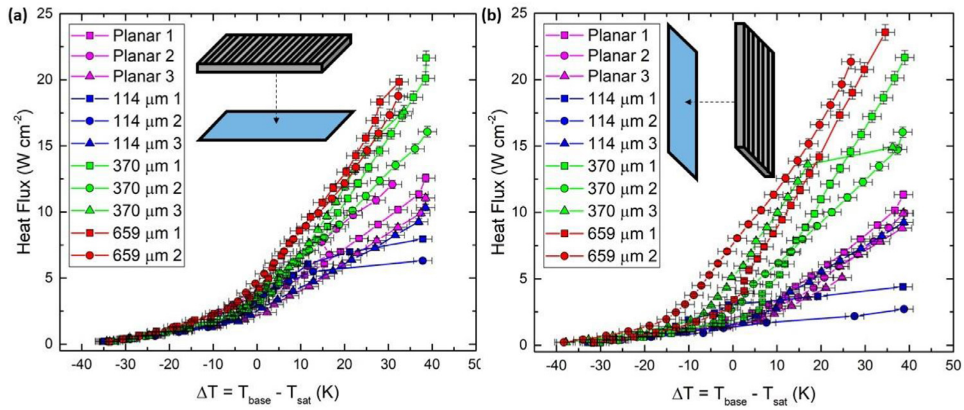

Fig. 5. Pool boiling performance curves for 40 K subcooled HFE-7100 using the projected base area (blue regions as shown in insets) of the MFAs to calculate heat flux. Plots are for the MFAs being in the (a) horizontal and (b) vertical orientations. Values in legend refer to fin height for each MFA, which is the differentiating feature between sample types For interpretation of the references to color in this figure legend, the reader is referred to the web version of this article..

patterning does not necessarily improve overall surface heat transfer performance in nucleate pool boiling scenarios with microscale features present. Unlike macroscopic systems where a generally uniform heat transfer coefficient is often assumed to act on all facets of an exposed surface, here there are complex transport phenomena including strong natural convection currents, bubble ebullition cycles, and bubble migration at work which microscale features can positively or negatively influence. More will be said on this point later in the discussion of high-speed video observations which goes deeper into explaining the bubble-level dynamics which underly the relatively poor surface-level performance of the 114 μm MFA samples.

In contrast to the shortest MFA samples, the taller MFAs with fin heights of 370 and 659 μm did show substantially better pool boiling performance than the baseline samples for both orientations. At ΔT~30 K, for example, the 659 μm MFAs' heat flux values were roughly double the average value observed for the baseline samples. Data gathering at the highest values of $\Delta T > 30$ K for the 659 μm MFAs was prevented by frequent heater burnout occurring for heat flux values of approximately 20 W cm^{-2} or slightly greater across all MFA sample types. This was due to the nichrome wire which comprises the heaters reaching its maximum power density. On average, the 659 μm MFAs outperformed the 370 μm MFAs. However, there was overlap within experimental uncertainty between the worst performing 659 μm MFA sample and the best performing 370 μm MFA sample. This indicates that the sample-to-sample variation was greater than the average benefit of taller fins, even though the 659 μm MFAs are ~1.8x taller and have ~1.44x greater surface area. This again points to phenomena occurring at the micro-fin level that prevent simple prediction of MFA performance by scaling either microfin height or surface area. In terms of orientation effects, ~10% greater heat flux was observed for the 370 and 659 μm MFAs at high ΔT for the vertical orientation as compared to the horizontal. This then leads to a somewhat greater performance enhancement over the baseline and 114 mm MFA samples, where no such gains were observed and performance was comparable or worse than in the horizontal. It is also important to note the sample-to-sample variation between MFAs of the same micro-fin height. This may be due to sub-micron differences induced during the roll molding process, but should be investigated and resolved in future work in order to give more predictable performance if widespread technological adoption is the eventual goal.

Fig. 5 and its associated discussion all feature heat flux values calculated using the projected base area, which was the same (25.4 x 25.4 mm) for all samples. It is also instructive to replot the data using the wetted surface area for each sample, in which case the numerical values for surface area are enhanced for each MFA sample type as given in Table 1. The result of this change in area basis is shown in Fig. 6 for both stage orientations. Interestingly, in the horizontal orientation the data for the two tallest MFA sample types are somewhat below that for the unpatterned planar baseline samples. In addition, the data for the 659 μm MFAs is somewhat below that of the 370 μm MFAs. These observations correlate with our statements previously about the lack of direct scaling of pool boiling performance with fin height and surface area. While the overall surface-level pool boiling performance may improve with increasing micro-fin height up to a point, the per unit wetted area performance actually degrades compared to the planar baseline case with increasing micro-fin height. This again suggests that there are changes occurring within the multiphase physics as the micro-fin height is altered, and that further increases in fin height may pay diminishing returns in terms of overall surface performance. Thus, the bubble dynamics and multiphase interactions at the micro-fin level must be understood in order to design and optimize MFA performance in a more intelligent manner.

These observations become even more apparent if the data of Fig. 6 is used to calculate the average heat transfer coefficient $h_{avg} = q_{wa}'' (T_s\text{-}T_\infty)^{-1}$ at each data point, where q_{wa}'' is the wetted surface area heat flux, T_s is the surface temperature, and T_∞ is the far-field pool temperature. Here, T_s is determined from the T_{base} experimental data by calculating the temperature drop across the aluminum base's thickness using 1D Fourier's Law based on the applied backside heat flux for each data point. This temperature drop was found to be less than 1.5 °C for the highest heat flux values. The result of this reprocessing is presented in Fig. 7. The magnitude of h_{avg} is in agreement with those typically associated with a working fluid such as the HFE-7100 used here and which have been previously reported [36], specifically ~200 – 500 W m^{-2} K^{-1} for natural convection and ~1000 W m^{-2} K^{-1} or greater for fully active pool boiling. This reprocessing shows that for the horizontal orientation at ΔT values below 10 K, the h_{avg} values are actually greatest for the baseline planar samples, then get progressively smaller with increasing micro-fin height. From this perspective, the 114 μm MFAs actually have superior performance than MFAs of greater fin height. It is now even more clear that there are micro-fin level phenomena which are reducing the wetted area basis heat transfer and that any gains in overall surface performance as seen in Fig. 5 must occur when the increase in surface area counteracts these micro-fin level reductions in h_{avg}. The range of h_{avg} observed for the vertical orientation are comparable to those seen for the horizontal orientation but without such a clear de-

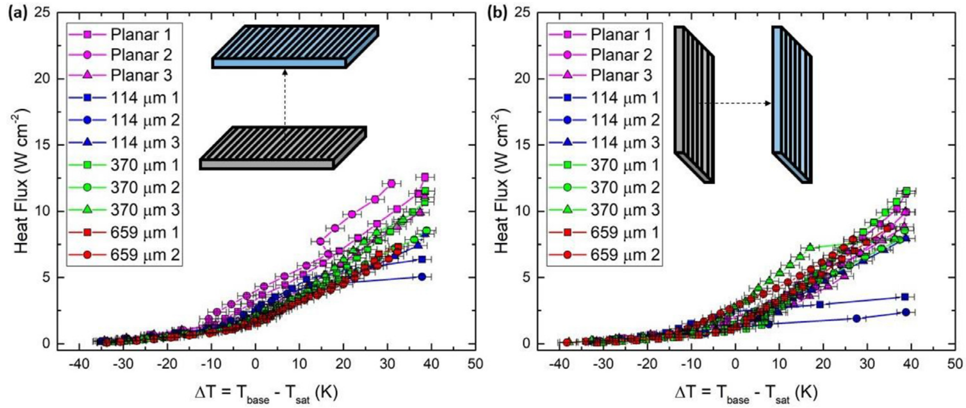

Fig. 6. Pool boiling performance curves for 40 K subcooled HFE-7100 using the wetted surface area (blue regions as shown in insets) of the MFAs to calculate heat flux. Plots are for the MFAs being in the (a) horizontal and (b) vertical orientations. Values in legend refer to fin height for each MFA, which is the differentiating feature between sample types For interpretation of the references to color in this figure legend, the reader is referred to the web version of this article..

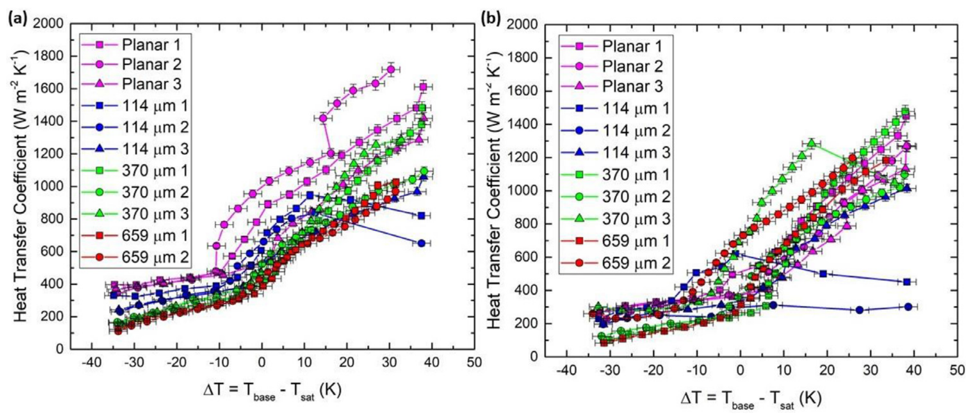

Fig. 7. Average heat transfer coefficient determined from the data presented in Fig. 5. Plots are for the MFAs being in the (a) horizontal and (b) vertical orientations. Values in legend refer to fin height for each MFA, which is the differentiating feature between sample types.

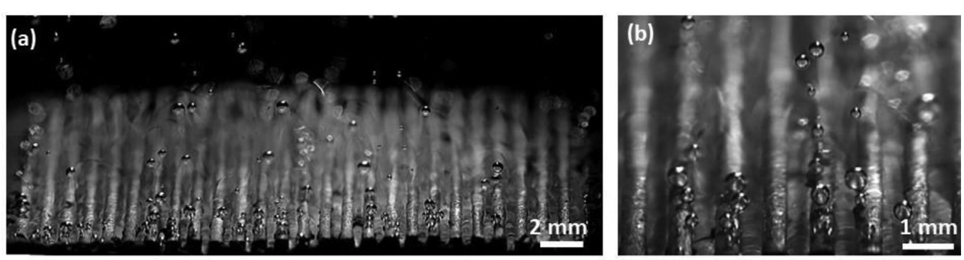

Fig. 8. Single frames taken from high-speed video showing bubble locations to be almost exclusively on micro-fin tops with MFA in horizontal orientation: (a) full sample view; (b) detailed view. The images are captured from 4000 fps video with a 240 μs exposure time.

pendency on MFA geometry. More will be said on this difference between the two orientations during the discussion of bubble dynamics observed from high-speed imaging.

4. Discussion

In order to better understand the apparent lack of clear scaling between surface area and heat transfer performance noted above, the bubble dynamics at the micro-fin level were observed via high-speed video during experiments. We present first the observations and associated discussion for horizontally orientated MFAs before contrasting with those for vertically oriented MFAs. As shown in **Fig. 8**, it was first noted that the vast majority of bubbles seen in a given frame resided on the micro-fin tops, with few if any seen within the micro-channel regions between micro-fins. This supports the idea that the microscale surface structuring with micro-fin and micro-channel dimensions comparable to the bubble departure diameter and capillary length comparable to the pattern pitch creates separate, repeating regions of differing liquid and vapor flow behavior across the sample surface.

Our hypothesis as to how and why such spatial periodicity and vapor bubble location specificity might occur is best explained by examining high speed images taken throughout a full pool boiling experiment, starting at low superheat values within the natural convection regime as shown in **Fig. 9**. At low superheat values where natural convection occurs, due to the difference in material thickness between the micro-fin regions and the micro-channel regions the bottom of the micro-channels will have a higher temperature than the tops of the micro-fins. We conservatively estimate this difference to be small but not insignificant, on the order of ~1 K based on a simple thermal resistance model. This cre-

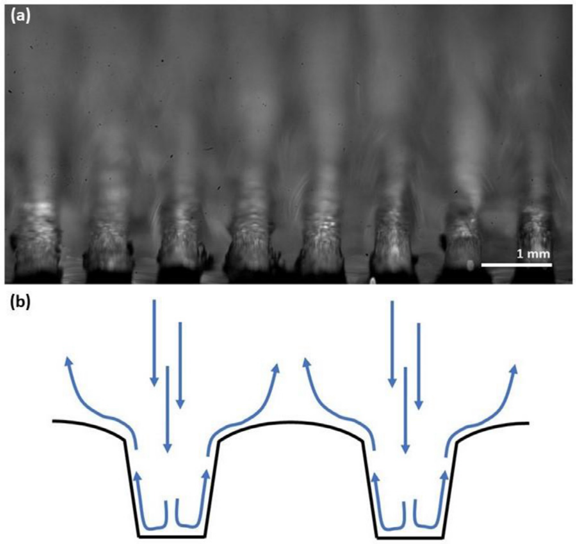

Fig. 9. (a) Single frames taken from high-speed video showing natural convection flow patterns from MFA topology in horizontal orientation. The image was captured from 2000 fps video with a 200 μs exposure time; (b) conceptual illustration of the proposed periodic bi-directional flow induced by the presence of the micro-fins, with impinging jet-like action near micro-channel centers (not to scale).

ates a net upward movement of fluid flow from the hotter micro-channel regions and micro-fin sidewalls, which curve around the top edges of each micro-fin. Such flow features can be seen in Fig. 9**(a)** in the vicinity of each individual micro-channel/micro-fin pairing. This net upward motion with slight lateral flow towards the center of each micro-fin leads to a need for replenishment of cooler fluid from the pool. We hypothesize that this comes in the form of a net downward flow occurring above each micro-channel region. Once established, this then forms alternating regions of upward flow from micro-fin tops and downward flow towards the center of each micro-channel, with the latter similar to an impinging jet action. This is illustrated conceptually in Fig. 9**(b)**. The dual flow direction hypothesis is supported via velocity vector results from the numerical model. Fig. 10**(a)** shows the velocity vectors of the warmer HFE-7100 with strong upward orientation, its migration up the sidewalls, and departure from the top surfaces of the MFA. The velocity vectors for the cooler liquid point downwards, filling up the space between micro-fins as shown in Fig. 10**(b)**. This illustrates the types of dual flow directions being driven by differential surface temperature and buoyancy effects. While we show representative results in Fig. 10**(b)** for an MFA with 659 µm tall micro-fins, this numerical observation is replicated in all simulations with the variation in micro-fin height.

The separated regions of upward and downward single-phase flow originating at low superheats have a strong influence on bubble nucleation behavior once it begins. At medium superheat values, vapor bubble nucleation was indeed observed to first begin at the bottom surfaces of the micro-channels. This is supportive of the idea that these are the hottest regions of the MFA. However, the high-speed videos also show that these bubbles quickly migrate to micro-fin tops shortly after nucleation. Similar vapor bubble migration behavior has been previously reported in the literature for silicon micro-channels with water as the working fluid, and for which spatially periodic flow patterns with the micro-channels primarily serving as liquid resupply pathways was pointed to as a root cause [9]. Similarly, it is here hypothesized that the combination of downward fluid flow near the micro-channel center and upward flow along micro-fin sidewalls forces the newly nucleated vapor bubble to move left or right depending on its nucleation location, where the liquid flow up the sidewall and the bubble's own buoyancy force F_b promote its migration to the micro-fin top. Once there, as observed via high-speed video, the vapor bubble first slides/oscillates along the micro-fin top due to the momentum associated with its rapid climb up the micro-fin sidewall. Upon stabilizing near the micro-fin center, the bubble is able to grow in size and depart. This complex sequence of events is depicted in the series of images given in Fig. 11 and illustrated conceptually in Fig. 12. While we present a single representative instance in Fig. 11, this behavior was observed to happen for almost all vapor bubbles visible during experiments. The bubble stabilization near the center of the micro-fin top is indicative that it finds a region of still or at least balanced local flow in this region where it is free to complete its growth and departure. As noted in the caption of Fig. 11, the entire sequence of events from first observation of nucleation to bubble departure covers less than 500 ms of time. However, the bubble migration from micro-channel bottom, up the micro-fin sidewall, and finally to the micro-fin top takes only about 1/10th of this time. Thus, bubble migration is relatively rapid compared to the full bubble ebullition cycle. The departing bubble also causes local convection within the fluid, which may further promote the cyclical flow pattern of upward flow from micro-fin tops.

As the degree of superheat increases, the temperature at the micro-fin tops eventually becomes high enough that nucleation activity begins here as well. Increased rate of departure of vapor bubbles from the micro-fin tops speeds up the need for replenishment from liquid regions, which in turn speeds up the flow of liquid being supplied via the micro-channel areas. This faster downward flow, similar to an impinging jet, works to further discourage vapor bubble nucleation and growth within the micro-channel regions [14]. Together, these phenomena are proposed to lead the scenario shown in Fig. 8 in which bubble locations were observed to be almost exclusively on micro-fin tops across the entire MFA. From automated image processing of still images obtained via high-speed video, the average bubble departure diameter was 319 μm, with a standard deviation of 51 μm. Departure diameter varied by less than 10% across all superheat values within the individual bubble nucleate boiling regime where such imaging was possible (up to approximately 12 W cm^{-2}). Thus, the observed average bubble departure diameter was somewhat larger than the micro-channel widths shown in Fig. 1.

The physical observations regarding natural convection and vapor bubble migration made from the high-speed video imaging can now help explain the measured pool boiling performance of the MFAs with varying micro-fin height. It was previously shown that there is a lack of direct scaling of pool boiling performance with fin height and, correspondingly, surface area. While the overall surface-level pool boiling performance was shown to improve with increasing micro-fin height up to those measured here (Fig. 5), the per unit wetted area performance actually degraded compared to the planar baseline case with increasing micro-fin height (Fig. 6). Further, relatively poor surface-level performance was seen from the 114 μm MFA samples in comparison to the planar baseline case despite its greater wetted surface area. Here, we hypothesize that the presence of micro-fins disrupts the normally unconstrained natural convection and rewetting pathways available on a planar, unpatterned surface. The observed early transition towards CHF-like behavior also points to strongly insufficient rewetting occurring for these samples. For short micro-fin heights such as for the 114 μm MFA samples, any benefits associated with the presence of the micro-fins such as an increase in surface area is not sufficient to overcome the negative implications of these flow pathway disruptions. In contrast, significant improvement in pool boiling performance compared to planar baseline was measured for the MFAs of tall micro-fin height (370 and 659 μm). This

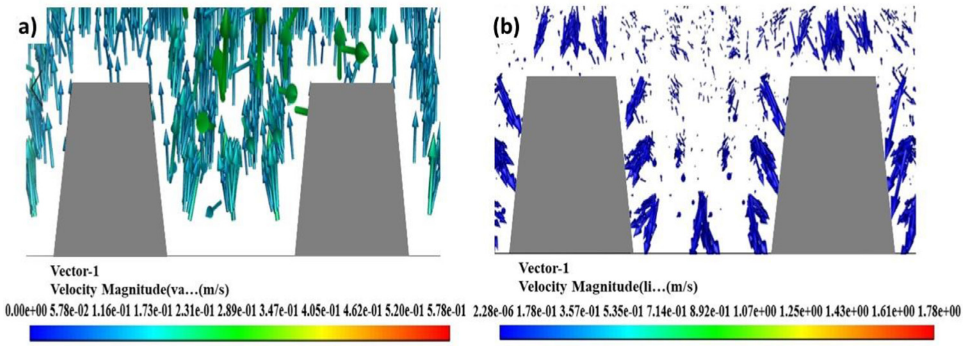

Fig. 10. Velocity vector results for MFA with 659 µm tall micro-fins showing dual flow directions for (a) vapor ($T > T_{sat}$) and (b) liquid ($T < T_{sat}$) HFE-7100 being driven by differential surface temperature and buoyancy effects. The scale for the arrows is 1:1.

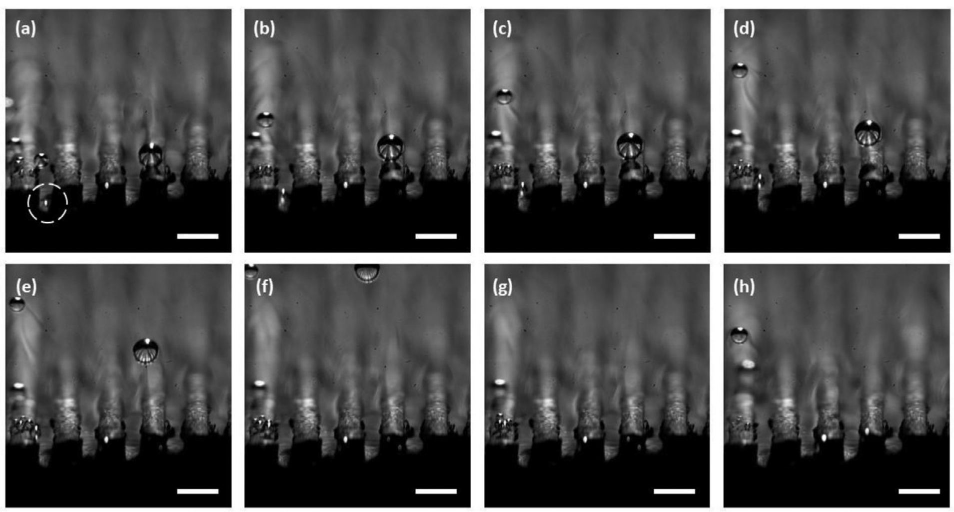

Fig. 11. Sequence of images demonstrating observed sequence of vapor bubble *(a)* nucleation within a micro-channel region, (*b–g)* migration to micro-fin tip, and *(h)* eventual departure. Vapor bubble in question is circled in the first frame for emphasis. White scale bars in each image are 1 mm. These images were captured from 3000 fps video with a 330 μs exposure time. The entire sequence of images covers a 470 ms duration, but the bubble migration shown in (b–g) occur over only 43 ms. Thus, bubble migration is relatively rapid compared to the full bubble ebullition cycle time.

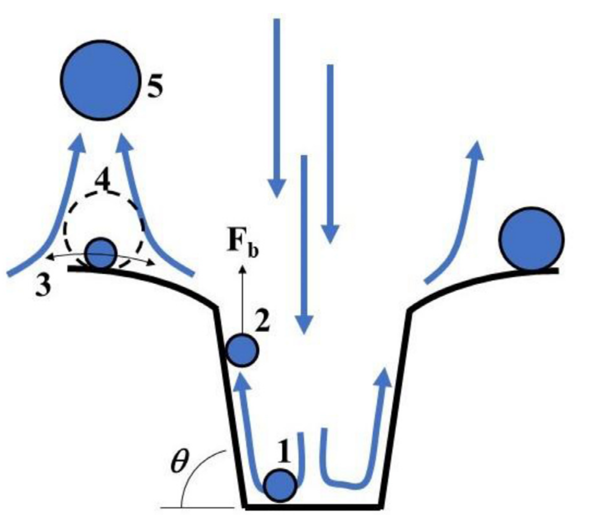

Fig. 12. Conceptual illustration of vapor bubble migration action consisting of 1. nucleation; 2. migration up microchannel sidewall; 3. oscillation on micro-fin top; 4. stabilization and growth; 5. departure. Illustration not to scale.

points to a critical conclusion that there must be a critical micro-fin height above which the pool boiling performance is improved by the induced periodic micro-flows along the surface and below which the presence of the micro-fins becomes a detriment.

While the pool boiling data supports this conclusion, what is less clear is what happens as micro-fin height continues to increase beyond the critical point. As noted previously, there was overlap within experimental uncertainty between the worst performing 659 μm MFA sample and the best performing 370 μm MFA sample. This indicates that the sample-to-sample variation was greater than the average benefit of taller fins, even though the 659 μm MFAs are ~1.8x taller and have ~1.44x greater surface area. It is possible that beyond an optimal micro-fin height, taller micro-fins make it more difficult for fluid from within the micro-channel regions to flow up the side walls and replenish regions on the micro-fin top where vapor bubbles are departing from. If true, in this scenario one would expect diminishing returns in terms of pool boiling heat transfer performance beyond an optimal micro-fin height.

Further study across a greater number of micro-fin heights within the range measured here is required to explore this behavior more fully and develop a clearer picture of how micro-fin height can be truly optimized for a given working fluid. This type of parametric optimization may best be performed using numerical modeling before choosing select cases for experimental verification. A similar need exists for exploring the effect of micro-fin spacing/micro-channel width on the types of spatially periodic

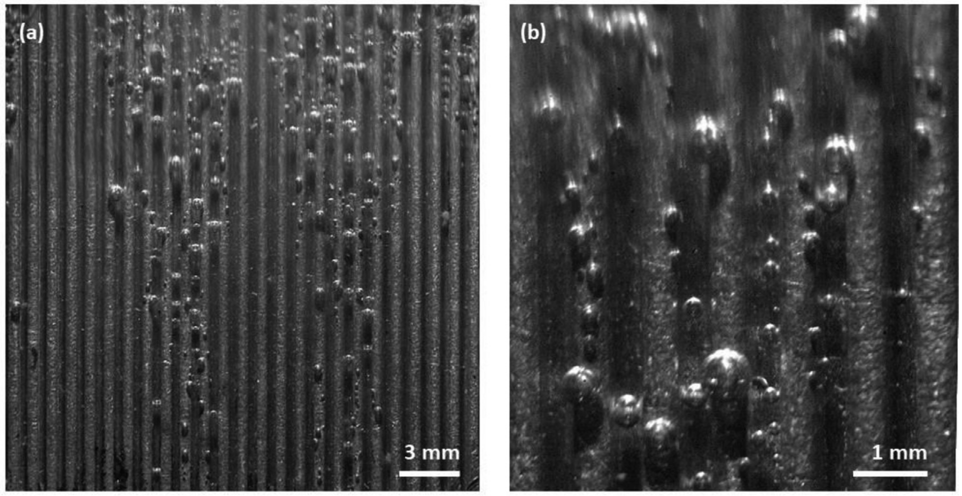

Fig. 13. Single frames taken from high-speed video showing bubble behavior for a vertically oriented MFA: (a) full sample view; (b) detailed view. The images were captured from 4000 fps video with a 240 μs exposure time.

micro-flow behavior observed to be induced via the presence of the micro-fins (**Figs. 9** and **12**). As micro-channel width increases, it is expected that a transition to more macroscopic-like unconstrained convection and bubble nucleation behavior should occur and that multiple regions of downward and upward flow may form between pairs of micro-fins. However, the specific micro-channel width at which this transition occurs and how it relates to other critical length scales such as bubble diameter and capillary length of the working fluid needs to be determined. From an application perspective in terms of optimizing pool boiling performance from MFAs, it is clear that the flow patterns, bubble dynamics, and multiphase interactions at the micro-fin level must be better understood in order to intelligently design and optimize MFA performance.

The above discussion on the complex, multi-faceted aspects of liquid and vapor bubble behavior on horizontally oriented MFAs was made possible in large part due to the ability to record high-speed video from an advantageous viewing perspective nearly parallel to the direction of the micro-fins. For vertically oriented MFAs, this viewing perspective was not available and imaging was performed perpendicular to the plane of the MFAs as shown in **Fig. 13**. However, some useful observations can still be made and linked to the measured pool boiling performance. In general, vapor bubbles were observed to nucleate nearly uniformly across the surface, beginning with small diameters and growing as they race upwards with convective currents, merge with other bubbles and increase their buoyancy. Although bubble nucleation was observed from all surface types (micro-channel bottoms, sidewalls, and micro-fin tops), many vapor bubbles were observed to prefer to move upwards either along micro-fin tops or spanning the space across a given micro-channel with attachment points bridging between micro-fins. Few if any were observed to move upwards entirely within a micro-channel's interior. This may be due to the vapor bubbles preferring the lower flow resistance offered by the regions on or near the tops of micro-fins.

In terms of the dual flow direction behavior associated with horizontally oriented 1D MFAs illustrated in **Figs. 9** and **12**, such effects were not observed and are unlikely for vertically orientated 1D MFAs. For the horizontal orientation, the hotter fluid from within the microchannels becomes more buoyant and the induced flow is perpendicular to the plane of the microchannels and microfin tops (**Fig. 9**). For the vertical orientation, while it is true that the microchannel bottoms would still be the hottest surfaces, the gravity vector is instead aligned with the microchannel direction. Hence, the direction of the buoyancy-driven flow is now along the microchannels and the microfin tops rather than perpendicular.

5. Conclusion

In this work, it was shown that the presence of D MFAs can significantly enhance pool boiling heat transfer performance above that of a planar, unpatterned baseline surface by as much as doubling the heat flux at the same degree of superheat for the best performing MFA samples. However, experimental data also demonstrated that a simple increase in surface area does not necessarily correlate to improved heat transfer performance as indicated by inferior performance from MFA samples with the shortest micro-fin height. These results were linked to observations made through high-speed imaging in which alternating regions of upward and downward flow were found to occur and were hypothesized to be a direct result of the presence of the 1D MFA patterning. Observations of distinct vapor bubble location preferences and migration behavior were also ascribed to the periodic multiphase elements induced by the presence of the micro-fins/micro-channels. Future work should seek to explore the effect of both micro-fin height and spacing on these flow patterns, as the findings presented in this work suggests that the optimal value of both may not be easily obtained *a priori* without an improved understanding of the multiphase behavior at the individual micro-fin level. These results expand the range of surface types (1D trapezoidal fins created through high throughput roll molding) and working fluids (low surface tension dielectric coolant) for which spatially periodic and distinct liquid/vapor transport pathways created via microscale surface modification have been reported. Importantly, the 1D Al alloy MFAs in this work are created via a high-throughput roll molding technique and possess superior scalability compared to other MFA fabrication methods, which helps address a key issue limiting the industrial adoption of micro/nanoscale surface modifiers.

Declaration of Competing Interest

The authors declare that they have no known competing financial interests or personal relationships that could have appeared to influence the work reported in this paper.

CRediT authorship contribution statement

Brendon Doran: Investigation, Writing – original draft. **Bin Zhang:** Investigation, Writing – original draft. **Shayan Davani:** Investigation, Writing – original draft. **Kojo Asiamah Osafo:** Formal analysis, Writing – original draft. **Owen Sutka:** Software. **Abigail Walker:** Software. **Nicholas Mueller:** Methodology. **Stephen Akwaboa:** Methodology, Writing – review & editing. **Patrick Mensah:** Conceptualization, Writing – review & editing. **W.J. Meng:** Conceptualization. **Arden L. Moore:** Conceptualization, Writing – review & editing.

Acknowledgments

The authors gratefully acknowledge support from the National Science Foundation through cooperative agreement OIA-1541079 and the Louisiana Board of Regents. This material is also based upon work supported by the National Science Foundation under Grant No. 1846165. Additional support for A. W. provided through a Louisiana Board of Regents Supervised Undergraduate Research Experience grant, Contract No. LEQSF-EPS(2018)-SURE-199.

References

[1] D. Attinger, C. Frankiewicz, A.R. Betz, T.M. Schutzius, R. Ganguly, A. Das, et al., Surface engineering for phase change heat transfer: a review, MRS Energy Sustain. 1 (2014) E4.
[2] S. Bhavnani, V. Narayanan, W. Qu, M. Jensen, S. Kandlikar, J. Kim, et al., Boiling augmentation with micro/nanostructured surfaces: current status and research outlook, Nanoscale Microscale Thermophys. Eng. 18 (2014) 197–222.
[3] D.E. Kim, D.I. Yu, D.W. Jerng, M.H. Kim, H.S. Ahn, Review of boiling heat transfer enhancement on micro/nanostructured surfaces, Exp Therm. Fluid Sci. 66 (2015) 173–196.
[4] K.C. Leong, J.Y. Ho, K.K. Wong, A critical review of pool and flow boiling heat transfer of dielectric fluids on enhanced surfaces, Appl. Therm. Eng. 112 (2017) 999–1019.
[5] M. McCarthy, K. Gerasopoulos, S.C. Maroo, A.J. Hart, Materials, fabrication, and manufacturing of micro/nanostructured surfaces for phase-change heat transfer enhancement, Nanoscale Microscale Thermophys. Eng. 18 (2014) 288–310 2014/07/03.
[6] C.Y. Lee, B.J. Zhang, K.J. Kim, Morphological change of plain and nano-porous surfaces during boiling and its effect on nucleate pool boiling heat transfer, Exp. Therm. Fluid Sci. 40 (2012) 150–158.
[7] H. Honda, J.J. Wei, Enhanced boiling heat transfer from electronic components by use of surface microstructures, Exp. Therm. Fluid Sci. 28 (2004) 159–169.
[8] G. Liang, I. Mudawar, Review of pool boiling enhancement by surface modification, Int. J. Heat Mass Transf. 128 (2019) 892–933 2019/01/01/.
[9] D. Cooke, S.G. Kandlikar, Pool boiling heat transfer and bubble dynamics over plain and enhanced microchannels, J. Heat Transf. 133 (2011).
[10] D. Cooke, S.G. Kandlikar, Effect of open microchannel geometry on pool boiling enhancement, Int. J. Heat Mass Transf. 55 (2012) 1004–1013 2012/01/31/.
[11] A. Jaikumar, S.G. Kandlikar, Enhanced pool boiling heat transfer mechanisms for selectively sintered open microchannels, Int. J. Heat Mass Transf. 88 (2015) 652–661 2015/09/01/.
[12] A. Jaikumar, S.G. Kandlikar, Pool boiling enhancement through bubble induced convective liquid flow in feeder microchannels, Appl. Phys. Lett. 108 (2016) 041604 2016/01/25.
[13] A. Jaikumar, S.G. Kandlikar, Ultra-high pool boiling performance and effect of channel width with selectively coated open microchannels, Int. J. Heat Mass Transf. 95 (2016) 795–805 2016/04/01/.
[14] A. Jaikumar, S.G. Kandlikar, Pool boiling inversion through bubble induced macroconvection, Appl. Phys. Lett. 110 (2017) 094107 2017/02/27.
[15] C.M. Patil, S.G. Kandlikar, Pool boiling enhancement through microporous coatings selectively electrodeposited on fin tops of open microchannels, Int. J. Heat Mass Transf. 79 (2014) 816–828 2014/12/01/.
[16] M.M. Rahman, J. Pollack, M. McCarthy, Increasing boiling heat transfer using low conductivity materials, Sci. Rep. 5 (2015) 13145 2015/08/18.
[17] M. Arik, A. Bar-Cohen, S.M. You, Enhancement of pool boiling critical heat flux in dielectric liquids by microporous coatings, Int. J. Heat Mass Transf. 50 (2007) 997–1009.
[18] R. Eiland, J.E. Fernandes, M. Vallejo, A. Siddarth, D. Agonafer, V. Mulay, Thermal performance and efficiency of a mineral oil immersed server over varied environmental operating conditions, J. Electron Packag. 139 (2018) 041005.
[19] B. Ramakrishnan, S.H. Bhavnani, J. Gess, R.W. Knight, D. Harris, R.W. Johnson, Effect of system and operational parameters on the performance of an immersion-cooled multichip module for high performance computing, Proceeding of the presented at the 2014 Semiconductor Thermal Measurement and Management Symposium (SEMI-THERM), San Jose, CA, 2014.
[20] S.V. Garimella, T. Persoons, J.A. Weibel, V. Gektin, Electronics thermal management in information communications technologies: challenges and future directions, IEEE Trans. Compon. Packag. Manuf. Technol. 7 (2017) 1191–1205.
[21] M.P. Groover, Fundamentals of Modern Manufacturing: Materials, Processes, and Systems, John Wiley & Sons, 2020.
[22] B. Lu, W.J. Meng, Roll molding of microchannel arrays on Al and Cu sheet metals: a method for high-throughput Manufacturing, J. Micro Nano-Manuf. 2 (2014) 011007.
[23] P.A. Primeaux, B. Zhang, X. Zhang, J. Miller, W.J. Meng, P. KC, et al., Aluminum-based one- and two-dimensional micro fin array structures: high--throughput fabrication and heat transfer testing, J. Micromech. Microeng. 27 (2017) 025012.
[24] A. Kalani and S.G. Kandlikar, "Pool boiling of FC-87 over microchannel surfaces at atmospheric pressure," presented at the ASME 2012 international mechanical engineering congress and exposition, 2012.
[25] A. Kalani, S.G. Kandlikar, Pool boiling heat transfer over microchannel surfaces with ethanol at atmospheric pressure, Proceeding of the Presented At the ASME 2012 10th International Conference on Nanochannels, Microchannels, and Minichannels, 2012.
[26] A. Kalani, S.G. Kandlikar, Enhanced pool boiling with ethanol at subatmospheric pressures for electronics cooling, J. Heat Transf. 135 (2013) 111002.
[27] C.K. Yu, D.C. Lu, Pool boiling heat transfer on horizontal rectangular fin array in saturated FC-72, Int. J. Heat Mass Transf. 50 (2007) 3624–3637 2007/08/01/.
[28] B. Doran, B. Zhang, A. Walker, P. Kc, W.J. Meng, A.L. Moore, Experimental determination of the role of increased surface area in pool boiling from nanostructured surfaces, Exp. Thermal Fluid Sci. 111 (2020) 109956 2020/02/01/.
[29] R.S. Figliola, D.E. Beasley, Theory and Design for Mechanical Measurements, John Wiley & Sons, Inc., New York, 2000 3rd Ed..
[30] I. Mudawar, T.M. Anderson, Optimization of enhanced surfaces for high flux chip cooling by pool boiling, J. Electron. Packag. 115 (1993) 89–100.
[31] F. Demiray, J. Kim, Microscale heat transfer measurements during pool boiling of FC-72: effect of subcooling, Int. J. Heat Mass Transf. 47 (2004) 3257–3268.
[32] M.S. El-Genk, H. Bostanci, Combined effects of subcooling and surface orientation on pool boiling of HFE-7100 from a simulated electronic chip, Exp. Heat Transf. 16 (2003) 281–301.
[33] J.L. Parker, M.S. El-Genk, Saturation and subcooled boiling of HFE-7100 on pinned surfaces at different orientations, J. Thermophys. Heat Transf. 23 (2009) 381–391 2009/04/01.
[34] K.N. Rainey, S.M. You, S. Lee, Effect of pressure, subcooling, and dissolved gas on pool boiling heat transfer from microporous, square pin-finned surfaces in FC-72, Int J. Heat Mass Transf. 46 (2003) 23–35.
[35] R.C. Gonzalez, R.E. Woods, Digital Image Processing, 4th Ed., Pearson, 2017.
[36] R.E. Simons, Direct liquid immersion cooling for high power density microelectronics, Electron. Cool. 2 (1996) 1–5.
[37] ANSYS, "ANSYS Fluent theory guide," 2013.
[38] S.N. Fincher, Thesis: numerical simulations of boiling in dielectric fluid immersion cooling scenarios of high power electronics, Auburn (2014) https://etd.auburn.edu/handle/10415/4067.
[39] M. Lemmert, L.M. Chawla, Influence of Flow Velocity On Surface Boiling Heat Transfer Coefficient in Heat Transfer in Boiling, Academic Press and Hemisphere, New York, 1977.
[40] G. Kocamustafaogullari, M. Ishii, Foundation of the interfacial area transport equation and its closure relations, Int. J. Heat Mass Transf. 38 (3) (1995).